
DEEP GENERATIVE CLASSIFICATION OF BLOOD CELL MORPHOLOGY

Simon Deltadahl¹ Julian Gilbey¹ Christine Van Laer^{2,3} Nancy Boeckx^{2,4} Mathie Leers⁵

Tanya Freeman⁶ Laura Aiken⁶ Timothy Farren⁶ Matthew Smith⁶ Mohamad Zeina⁷

BloodCounts! consortium Concetta Piazzese^{6,8} Joseph Taylor^{6,8} Nicholas Gleadall⁹

Carola-Bibiane Schönlieb¹ Suthesh Sivapalaratnam^{6,8,†} Michael Roberts^{1,10,†} Parashkev Nachev^{7,†}

ABSTRACT

Accurate classification of haematological cells is critical for diagnosing blood disorders, but presents significant challenges for machine automation owing to the complexity of cell morphology, heterogeneities of biological, pathological, and imaging characteristics, and the imbalance of cell type frequencies. We introduce CytoDiffusion, a diffusion-based classifier that effectively models blood cell morphology, combining accurate classification with robust anomaly detection, resistance to distributional shifts, interpretability, data efficiency, and superhuman uncertainty quantification. Our approach outperforms state-of-the-art discriminative models in anomaly detection (AUC 0.976 vs. 0.919), resistance to domain shifts (85.85% vs. 74.38% balanced accuracy), and performance in low-data regimes (95.88% vs. 94.95% balanced accuracy). Notably, our model generates synthetic blood cell images that are nearly indistinguishable from real images, as demonstrated by a Turing test in which expert haematologists achieved only 52.3% accuracy (95% CI: [50.5%, 54.2%]). Furthermore, we enhance model explainability through the generation of directly interpretable counterfactual heatmaps. Our comprehensive evaluation framework, encompassing these multiple performance dimensions, establishes a new benchmark for medical image analysis in haematology, ultimately enabling improved diagnostic accuracy in clinical settings. Our code is available at <https://github.com/Deltadahl/CytoDiffusion>.

¹Department of Applied Mathematics and Theoretical Physics, University of Cambridge, Cambridge, UK

²Department of Laboratory Medicine, UZ Leuven, Leuven, Belgium

³Department of Cardiovascular Sciences, Center for Molecular and Vascular Biology, University of Leuven, Leuven, Belgium

⁴Department of Oncology, KU Leuven, Leuven, Belgium

⁵Zuyderland Medical Center, Sittard-Geleen, Netherlands

⁶Barts Health NHS Trust, London, United Kingdom

⁷Queen Square Institute of Neurology, University College London, London, UK

⁸Queen Mary University of London, London, United Kingdom

⁹Department of Haematology, University of Cambridge, Cambridge, UK

¹⁰Department of Medicine, University of Cambridge, Cambridge, UK

[†]Equal contribution

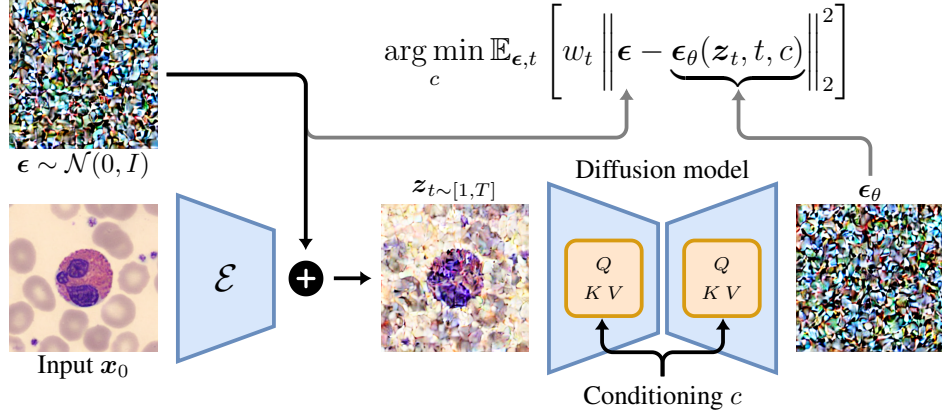


Figure 1: Representation of the diffusion-based classification process. An input image x_0 is first encoded into a latent space using an encoder \mathcal{E} . Gaussian noise $\epsilon \sim \mathcal{N}(0, I)$ is then added to create a noisy latent representation z_t . This noisy representation is fed through a diffusion model for each possible class condition c . The model predicts the noise ϵ_θ for each condition. The classification decision is made by selecting the class that minimises the error between the predicted noise ϵ_θ and the true noise ϵ .

The haematological is amongst the most complex of physiological systems, and uniquely intertwined with all others. Though often quantified by simple “blood counts” of cell class frequencies, its characteristics are both supremely rich and highly variable within and across individuals [1]. A cardinal aspect is the morphology of individual blood cells as seen on light microscopy of blood smears [2]. The richness of morphological appearances—and their complex modulation by diverse biological, pathological, and instrumental factors—demand human expert visual description in commensurately expressive terms. The allocation of a cell to its major morphological type, e.g. lymphocyte, is only the crudest form of description, on which finer fractionation into subtypes, across a wide spectrum of (ab)normality, is overlaid.

Indeed, the task of morphological characterisation is both open-ended and lacks a definitive ground truth: there may be morphological patterns whose subtlety has concealed great clinical significance, and some morphological classes are purely expert-determined visual phenotypes with no means of objective corroboration. Moreover, pathological appearances may be highly unusual or unique, precluding classification into any class, even at the simplest level of description, and requiring metacognitive awareness of its impossibility. The difficulty is commonly compounded by interactions with irrelevant biological features with variable representation across the population, and instrumental variations of technical origin [3, 4]. The challenge, in short, is one human experts can only imperfectly meet, inevitably exhibiting marked variation with skill and experience [5, 6].

So framed, the task of automating blood morphological analysis has a different aim from that commonly assumed, needs broader validation, and is harder to accomplish. The primary aim is not to approximate a human expert in a more cost-effective, reproducible, and scalable alternative, but to capture the space of possible morphological appearances with potentially superhuman fidelity, flexibility, and metacognitive awareness. It cannot plausibly be achieved by a discriminative model trained to classify cells into standard morphological classes, for such an approach can only approximate human fidelity, and is ill-equipped to deal with the domain shifts, class imbalances and anomalies, complex interactions between biological, pathological, and instrumental features, and metacognitive demands, that the foregoing implies. Nor can success in the task be evaluated by standard measures of in-distribution performance, for they are remote from real-world experience.

Here we therefore introduce a deep generative approach founded on diffusion-based classifiers, and a comprehensive evaluative framework that aspires to real-world ecological validity. Our approach, which we call CytoDiffusion, addresses the key challenges, exemplified by blood morphological analysis but not unique to it, of machine vision models of medical data, namely:

1. **Domain Shift:** Models trained on data from a specific biological, pathological, and instrumental context often struggle when applied to data with a different distribution of characteristics, limiting their practical utility [7, 8].
2. **Anomaly Detection:** The ability to identify rare or previously unseen patterns of features is crucial in clinical applications yet often overlooked in model development and evaluation [9]. Models should be capable of

recognising patterns absent from the training data, for such cases fall outside the model’s competence and must be so highlighted.

3. **Uncertainty Quantification:** Ideal epistemic agents—human or machine—can accurately quantify the reliability of their knowledge, exhibiting metacognitive awareness. Reliable uncertainty quantification is crucial for clinical decision-making, yet is widely neglected in model assessments [10]. The utility of a prediction depends on its uncertainty, and requires weighting by it, both in direct use and the design of ensemble-based systems.
4. **Data Heterogeneity and Incompleteness:** Many existing medical datasets fail to replicate the heterogeneity—biological, pathological, and instrumental—and incompleteness prevalent in real-world clinical life [11]. Generalisation to real-world scenarios is therefore inadequately tested.
5. **Interpretability:** In medical applications, the reasoning behind a model’s decisions may be as important as the decisions themselves, yet many current approaches lack interpretability [12, 13].
6. **Data efficiency:** The medical domain is constitutionally constrained in data scale, in numbers of cases in proportion to observed diversity and especially in ground truth labels. Successfully deployable models must therefore be data efficient.

While numerous studies have reported high accuracies in various medical image analysis tasks [14, 15, 16], these broader challenges remain largely unaddressed, limiting the clinical applicability of such models.

We apply diffusion-based classifiers to this real-world clinical challenge, building on recent work that has demonstrated their promising robustness to distribution shifts and ability to avoid shortcut solutions [17, 18, 19, 20]. CytoDiffusion offers several advantages, including improved robustness to domain shifts and inherent capabilities for anomaly detection and uncertainty quantification.

A key advantage of generative classifiers is their ability to model the input in its entirety, rather than relying on spurious correlations or shortcuts that traditional discriminative classifiers often exploit [17]. By learning to generate examples of each class, generative classifiers are forced to capture the full complexity of the input space.

In the context of blood cell classification, CytoDiffusion is compelled to learn the complete morphological characteristics of each cell type, rather than focusing on easily discriminative but potentially unreliable features. This holistic approach is particularly valuable in medical imaging, where subtle details can be crucial for accurate diagnosis. Figure 1 illustrates the operation of our proposed model.

Specifically, our contributions include:

1. A novel application of latent diffusion models for blood cell classification.
2. An evaluation framework that goes beyond accuracy, incorporating domain shift robustness, anomaly detection capability, and performance in low-data regimes.
3. A new dataset of blood cell images that includes artefacts and labeller confidence scores, addressing key limitations in existing datasets.
4. A principled framework for metacognitive evaluation of model and human confidence based on established psychometric modelling techniques.
5. A method for generating interpretable heatmaps to explain model decisions, crucial for validation.

Through these contributions, we aim to establish a new standard for the development and assessment of blood cell classification models. Our work addresses critical aspects of clinical applicability, including robustness, interpretability, and reliability.

We propose that the research community adopt these evaluation tasks and metrics when assessing new models for blood cell image classification. By going beyond simple accuracy measures, we can develop models that are not only high-performing but also trustworthy and clinically relevant.

1 Results

We begin by validating the quality of images generated by CytoDiffusion through a Turing test. Next, we assess the model’s in-domain performance on standard classification tasks across multiple datasets. We then examine CytoDiffusion’s ability to quantify uncertainty, comparing its metacognitive capabilities with those of human experts. Following this, we evaluate the model’s proficiency in anomaly detection, crucial for identifying rare or unseen cell types. We proceed to test the model’s robustness to domain shifts, simulating real-world variability in imaging conditions.

Subsequently, we investigate CytoDiffusion’s efficiency in low-data regimes, a critical consideration for medical applications where large, well-annotated datasets may be scarce. Finally, we demonstrate CytoDiffusion’s explainability through the generation of counterfactual heatmaps, providing interpretable insights into its decision-making process.

1.1 Turing test

To assess whether our fine-tuned diffusion model could effectively capture the distribution of blood cell images and demonstrate sufficient expressiveness, we designed a Turing test specifically adapted for peripheral blood film imaging. CytoDiffusion was trained on a dataset comprising 32,619 images. The results of our Turing test, which involved expert haematologists assessing the authenticity of the images, underscore the model’s capability to replicate the complex morphological characteristics of blood cells.

The 10 haematologists participating in the study evaluated a total of 288 images each, resulting in 2,880 individual assessments. They demonstrated an overall accuracy of 52.3%, 95% CI: [50.5%, 54.2%] in distinguishing between real and synthetic images, with a sensitivity of 55.8% and a specificity of 48.9%. This performance is comparable to random guessing, indicating that the synthetic images produced by CytoDiffusion are almost indistinguishable from real blood cell images, even to experienced professionals.

In addition to the Turing test, we evaluated the fidelity of blood cell type conditional synthesis. The haematologists’ classification of the synthetic images aligned with the model’s intended cell type with an agreement rate of 98.6%. Overall, these results affirm that CytoDiffusion not only generates high-quality synthetic images but also accurately captures the class-defining morphological features of blood cells (see Figure 8 in the supplementary material).

1.2 In-Domain Performance

To establish a baseline for our diffusion-based classifier, we evaluated CytoDiffusion’s performance on standard in-domain classification tasks. We used three datasets for this evaluation: our custom dataset, Raabin-WBC [21], and PBC [22]. Table 1 presents a comparison of our model against other methods that have been evaluated on these datasets.

CytoDiffusion demonstrates competitive performance across all datasets, particularly in balanced accuracy. This metric is especially relevant given the significant class imbalances present in these datasets. For instance, our custom dataset’s class distribution ranges from 103 to 1425 images per class, whilst Raabin-WBC TestA varies from 89 to 2660 images per class.

It is important to note that we have excluded some studies from our comparison due to methodological differences that could lead to unfair or misleading comparisons. Specifically, we are not comparing with papers that do not have a proper train-validation-test split [23, 24], or those that do not test on the predefined test set [16, 25].

1.3 Uncertainty Measure

The biological realm is characterised by constitutional, incompletely reducible uncertainty. In every task, it is valuable to quantify not only the fidelity but also the uncertainty of the agent: human or machine. Metacognitive measures of this kind enable qualification of predictions, stratification of case difficulty, and principled ensembling of agents [38, 39].

Our dataset uniquely incorporates labeller confidence for all images, providing a rare opportunity to compare model uncertainty with human expert uncertainty. This feature allows us to assess how well CytoDiffusion’s uncertainty aligns with that of experienced haematologists, offering valuable insights into the model’s ability to capture the nuances and complexities of cell classification. CytoDiffusion determines the error between the predicted and true noise for each class (see Figure 1). We take the difference between the two smallest errors to represent the confidence of the model: the larger the difference, the more confident the model is in its prediction.

An ideal agent’s epistemic uncertainty is equal to the system’s aleatoric uncertainty. The optimal relation between uncertainty and accuracy should therefore approximate that of an ideal psychophysical observer detecting a noisy signal [40]. Though we do not have independent quantification of the signal here, we can quantify how well the uncertainty measure conforms to a psychophysical model by treating it as if it were an index of task difficulty. We do this by employing Bayesian psychometric function estimation [41, 42] with the inverse of uncertainty–confidence—as the index of task difficulty, estimating the parameters of the resultant psychometric function for both individual experts and our model (Figure 2). Strikingly, whilst expert performance produces a noisy function (Figure 2C), CytoDiffusion conforms to the behaviour of a psychophysical observer with tight bounds on the posterior distributions of the key parameters of width and threshold (Figure 2A). This behaviour closely resembles that of an ideal observer, suggesting that our model’s epistemic uncertainty conforms to the structure of the aleatoric floor.

Table 1: Comparison of various methods on our custom dataset, the Raabin-WBC (TestA) dataset, and the PBC dataset. Best results are in bold, second-best are underlined. Balanced accuracy is reported where available.

Dataset	Method	Year	Accuracy (%)	Balanced Accuracy (%)
Ours	ViT-B/16	2024	84.42	76.89
	EfficientNetV2-M	2024	<u>85.74</u>	<u>80.69</u>
	CytoDiffusion (ours)	2024	86.48	85.27
Raabin-WBC TestA	Tavakoli et al. [26]	2021	94.65	92.76
	Kouzehkanan et al. [21]	2022	99.17	97.95
	Chen et al. [27]	2022	98.71	98.42
	Jiang et al. [28]	2022	95.17	91.71
	Rivas et al. [29]	2023	98.29	97.69
	Tsutsui et al. [30]	2023	98.75	-
	Li et al. [31]	2024	97.80	-
	ViT-B/16	2024	96.93	97.28
	EfficientNetV2-M	2024	<u>98.99</u>	<u>98.40</u>
	CytoDiffusion (ours)	2024	96.43	97.93
PBC	Acevedo et al. [22]	2019	96.20	96.16
	Ucar [32]	2020	97.94	97.94
	Rastogi et al. [33]	2022	92.00	91.46
	Ali et al. [34]	2023	93.00	91.00
	Manzari et al. [35]	2023	95.40	-
	Almalik et al. [36]	2023	93.60	-
	Tummala et al. [37]	2023	97.25	97.25
	Firat et al. [16]	2024	99.72	98.91
	ViT-B/16	2024	98.70	98.76
	EfficientNetV2-M	2024	99.17	<u>99.14</u>
	CytoDiffusion (ours)	2024	<u>99.35</u>	99.37

Indeed, CytoDiffusion produces arguably superior stratification of case difficulty than human experts themselves. Estimating functions of expert performance with model confidence as the index yields tighter fits, and enables better separation of experts differing in performance relative to the consensus ground truth (Figure 2B, D, E).

CytoDiffusion’s ability to quantify its own uncertainty accurately is crucial for clinical applications, as it allows for the identification of cases that may require additional expert review. This feature could significantly enhance the reliability and trustworthiness of automated blood cell classification systems in real-world clinical settings.

1.4 Anomaly Detection

To assess the model’s ability to distinguish between seen and unseen cell types, we require a metacognitive index of its confidence. The evaluation procedure involved two steps: first, training CytoDiffusion on datasets that omitted specific cell types; then, testing it on held-out sets that included these previously unseen cell types.

To quantify the model’s confidence, we use the measure described in Section 1.3. For normal cells (those present in the training data), we expect the model to be more confident in its top prediction, whilst for abnormal cells (those excluded from training), we expect less confidence.

We visualise these differences for normal and abnormal cells using kernel density estimates (KDE) in Figure 3, revealing a striking difference between the two distributions. To quantify this separation, we constructed receiver operating characteristic (ROC) curves for distinguishing normal from abnormal cells using the error difference. We then calculated the area under the ROC curve (AUC) to measure the model’s ability to differentiate between known and unknown cell types.

For the Bodzas dataset [43], with blasts as the abnormal class, we achieved an AUC of 0.971. The PBC dataset [22], using erythroblasts as abnormal, yielded an even higher AUC of 0.976. These high AUC values demonstrate our model’s capability to distinguish between normal cells it was trained on and abnormal cell types not present in the training data.

To put our results in perspective, we compared CytoDiffusion’s performance with a Vision Transformer (ViT-B/16) model. For the ViT, we used the difference between the two largest outputs in the logits (before the softmax) as a measure of confidence. The ViT achieved an AUC of 0.744 for the Bodzas dataset (blasts as abnormal) and 0.919 for

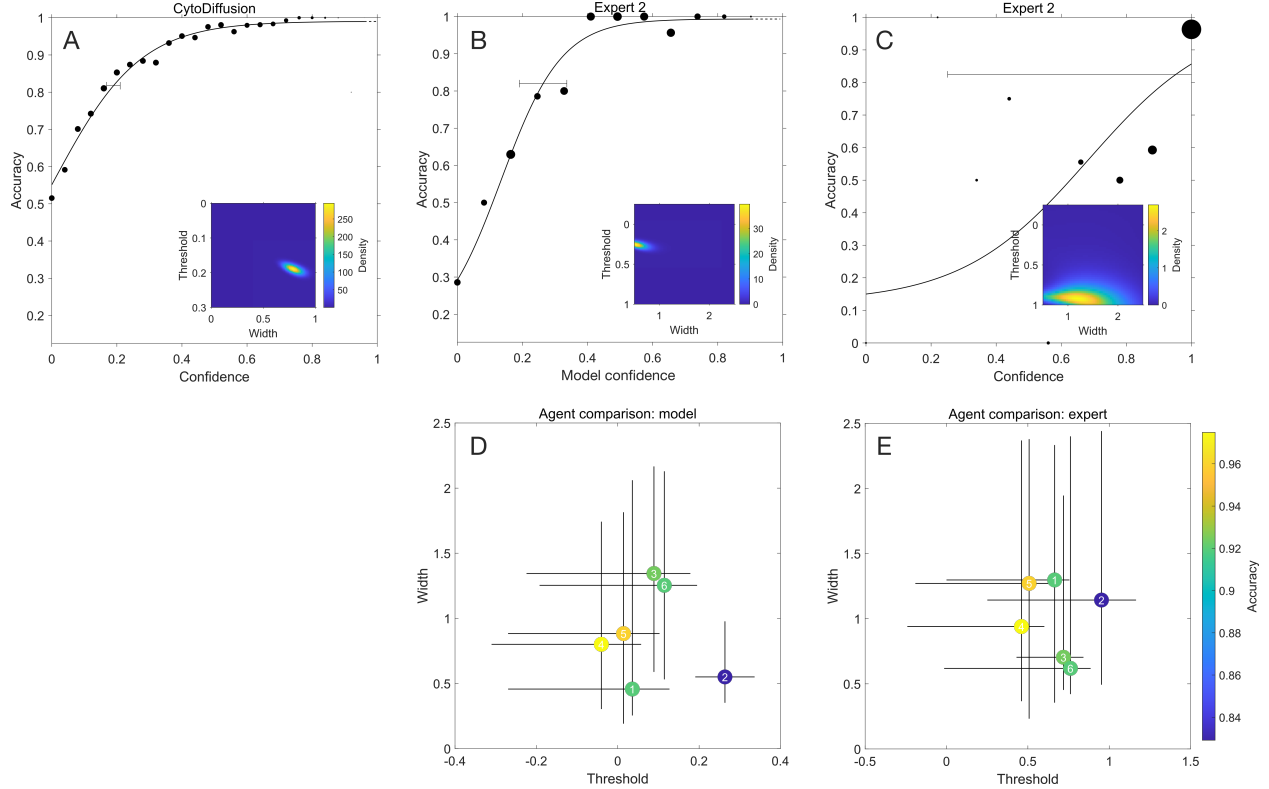


Figure 2: Bayesian psychometric analysis of model and expert performance. A. Psychometric function of CytoDiffusion’s performance on our custom dataset with model confidence as the index of signal strength. The 95% credibility interval of the threshold of the function, estimated at the point of 80% correct unscaled by lapse and guess rate, is shown as an error bar, and the posterior distributions of threshold and width are presented in the inset axes. Note tight bounds on the parameters. B. Psychometric function of the performance of a single human expert, derived from a randomly selected subset of 200 cases for which a consensus ground truth is available, with model confidence as the index of signal strength. C. Psychometric function of the expert shown in B, with consensus expert confidence as the index of signal strength. D & E. Width and threshold parameter estimates and their 95% credibility intervals for each of the six human experts with model confidence (D) and consensus expert confidence (E) as the indices of signal strength.

the PBC dataset (erythroblasts as abnormal). While the ViT demonstrates reasonable performance, particularly for the PBC dataset, our diffusion-based model consistently outperforms it, showing superior capability in detecting anomalous cell types.

This ability to identify rare or unexpected cell types is crucial in clinical settings, where the detection of abnormal cells can have significant diagnostic implications. We propose that future models report AUC scores for similar anomaly detection tasks, providing a standardised metric for assessing a model’s ability to flag potentially abnormal findings in medical imaging.

1.5 Domain Shift

The ability of a classification model to generalise across different imaging conditions is crucial for its practical application in clinical settings. This generalisation capability is particularly important in haematology, where variations in microscope types, camera systems, and staining techniques are common across different laboratories and hospitals. A model that performs well only under specific imaging conditions would have limited utility in real-world clinical practice, potentially leading to inconsistent or unreliable diagnoses when deployed in new environments.

We propose that new models in this domain should be evaluated on their performance under various domain shift scenarios to assess their robustness and adaptability. To demonstrate this evaluation approach, we conducted experiments using the Raabin-WBC dataset for training, with testing performed on two distinct datasets: TestB and LISC (see Table 3 for dataset details).

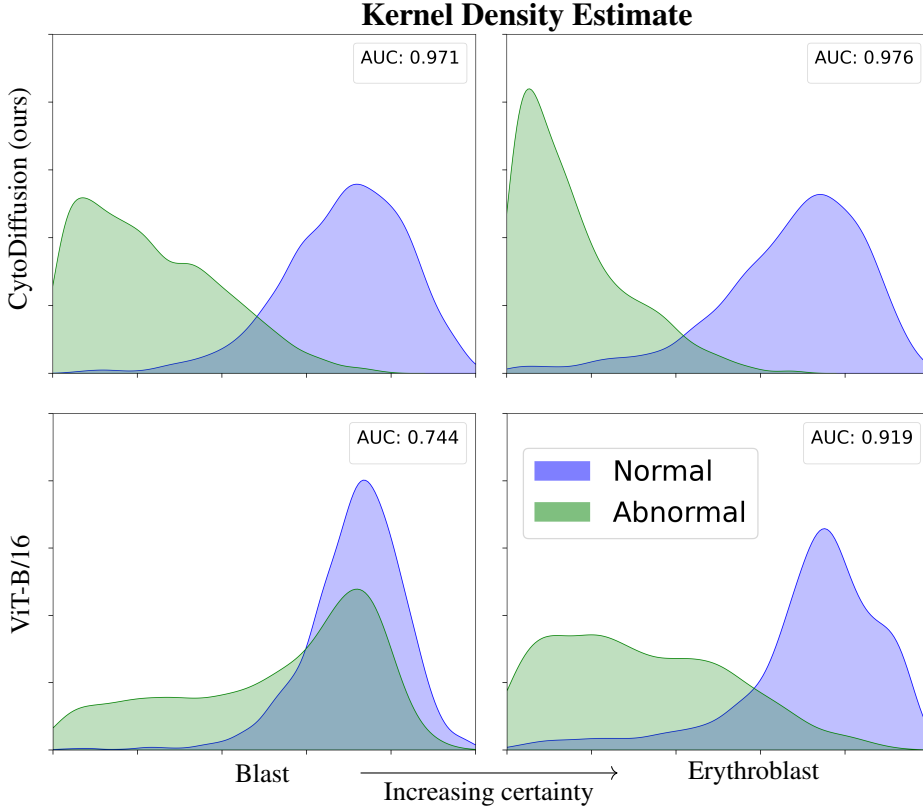


Figure 3: Kernel density estimate figures comparing the anomaly detection performance of our diffusion-based model (top row) with ViT-B/16 (bottom row) for blasts (left column) and erythroblasts (right column). The horizontal axis represents the certainty measure, normalised to $[0, 1]$ by dividing by the maximum certainty for each model and dataset. The AUC values indicate the model’s ability to distinguish between normal and abnormal samples.

TestB is part of the Raabin dataset, but the authors have provided a specific split for testing purposes. It differs from the training set in camera type and microscope type. LISC, on the other hand, introduces more significant shifts, differing in camera type, microscope type, and staining technique. Table 2 presents the results of our evaluation using this framework.

Table 2: Performance under domain shift conditions. Models were trained on the Raabin-WBC dataset and evaluated on TestB and LISC datasets, representing different degrees of domain shift. TestB differs from the training set in camera and microscope type, while LISC introduces additional variations in staining technique. Balanced accuracy scores (mean \pm standard deviation) from five independent training sessions are reported.

Method	TestB	LISC
Li and Liu [31]	92.36 ± 0.73	62.51 ± 2.83
Li and Liu [31]	86.84 ± 1.91	64.96 ± 2.63
S. Tsutsui [30]	92.98 ± 1.84	70.84 ± 6.10
ViT-B/16 [44]	96.75 ± 2.94	62.28 ± 14.47
EfficientNetV2-M [45]	96.91 ± 2.24	74.38 ± 4.87
CytoDiffusion (ours)	98.39 ± 0.34	85.85 ± 2.66

1.6 Efficiency in Low-Data Regimes

The ability of a model to perform well with limited training data is crucial in medical imaging contexts, where large, well-annotated datasets are often challenging to obtain. We propose that new models in this domain should be evaluated on their performance in low-data regimes to assess their efficiency.

To demonstrate this evaluation approach, we conducted experiments using the PBC dataset [22]. We compared the performance of multiple models, including our proposed approach CytoDiffusion, and two established architectures: EfficientNetV2-M [45] and ViT-B/16 [44]. The training was carried out with subsets of 10, 20, 50, and 150 images per class, simulating conditions of sparse data availability.

Figure 4 presents the results of these experiments, illustrating the balanced accuracy of each model as a function of the number of training images per class. Our proposed model consistently outperforms EfficientNetV2-M and ViT-B/16 across all data regimes, with the advantage particularly pronounced in the most data-scarce conditions.

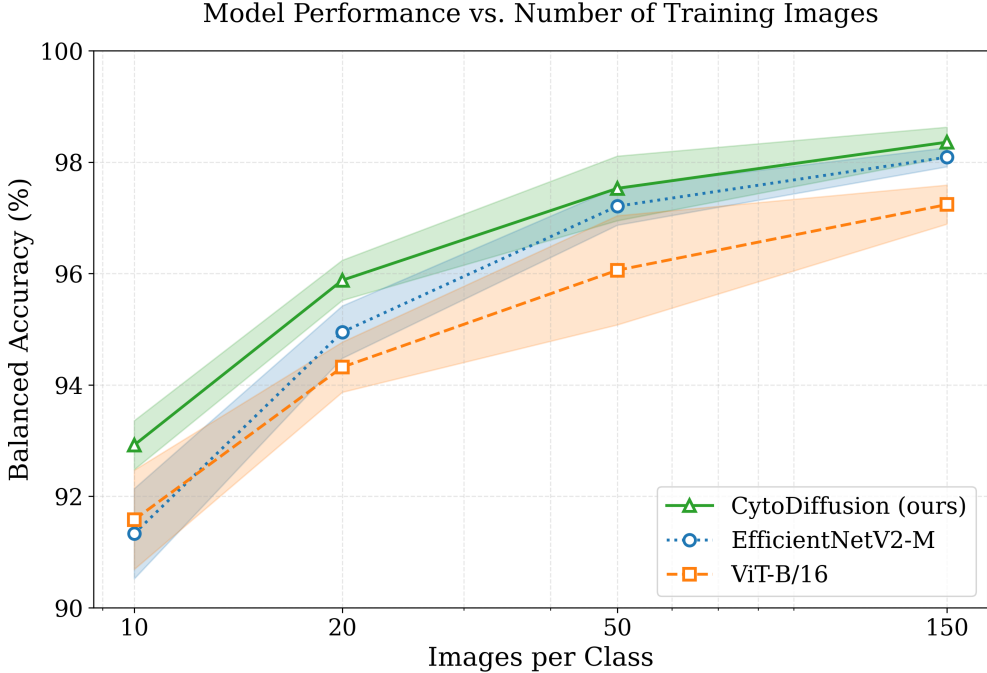


Figure 4: Model performance comparison under low-data conditions. The graph shows the balanced accuracy of our proposed model, EfficientNetV2-M, and ViT-B/16 as a function of the number of training images per class. Shaded areas represent the standard deviation from five independent training sessions.

1.7 Explainability

A crucial aspect of deploying machine learning models in clinical settings is their ability to provide interpretable results. CytoDiffusion addresses this need through the generation of counterfactual heatmaps, which highlight the regions of an image that would need to change for it to be classified as a different cell type. A distinctive feature of our approach is that these heatmaps are the direct output of our model, requiring no post-processing or additional colour mapping. This direct output capability preserves the integrity of the model’s decision-making rationale, offering an unfiltered view of its reasoning process.

Figure 5 illustrates this process using an eosinophil as an example. When the model is prompted to consider what alterations would be necessary for this cell to be classified as a neutrophil, it generates a heatmap ($H_{\text{neutrophil}}$) highlighting the key areas of difference. The overlay of this heatmap on the original image reveals that the model focuses primarily on distinguishing granularity between neutrophils and eosinophils. Eosinophils contain larger, spherical and mostly higher quantity of eosinophilic stained granules in comparison to neutrophils [46].

To provide a comprehensive view of our model’s reasoning across all cell types, we generated counterfactual heatmaps for each possible class transition in the PBC dataset (Figure 6). This visualisation offers insights into the model’s decision-making process for each cell type. For instance, when considering the transition from neutrophil to eosinophil (row 2, column 7), the model highlights regions in the cytoplasm (darker areas) where features should be added, while largely maintaining the nuclear shape.

Notably, the heatmaps also reveal the model’s understanding of subtle differences between similar cell types. In the transition from monocyte to immature granulocyte (Figure 6, row 4, column 6), the model indicates the difference in

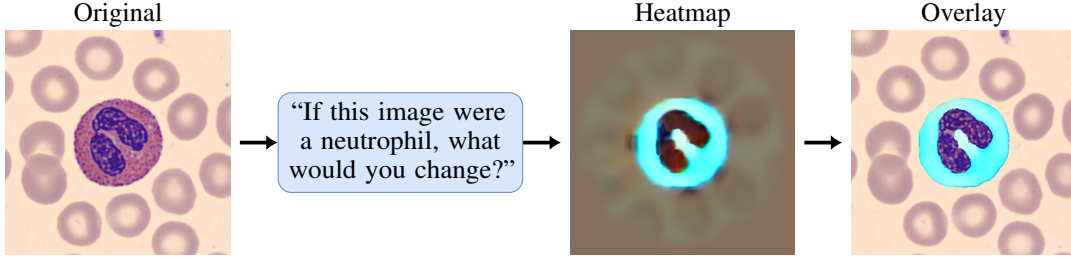


Figure 5: Counterfactual heatmap visualisation. Left: Original eosinophil image. Centre-right: Counterfactual heatmap ($H_{\text{neutrophil}}$) illustrating the areas that differ when the model considers the image as a neutrophil. Darker areas in the heatmaps indicate features to be added, whilst lighter areas suggest features to be removed to achieve the target cell type. Far right: Overlay of the thresholded heatmap on the original image, highlighting the most significant areas of difference, primarily in the granules.

cytoplasm between the more acidophilic cytoplasm of the immature granulocytes in comparison to the greyish-blue monocytic cytoplasm. Intriguingly, the model also suggests the filling of the monocytic vacuoles (appearing as dark spots in the heatmap). This captures one of the typical morphological findings in monocytes differentiating them from other normal blood cells and demonstrates the model’s ability to focus on nuanced information.

These results provide valuable insights into CytoDiffusion’s decision-making process, offering a detailed visualisation of the morphological distinctions the model identifies between cell types. This granular view of the model’s reasoning enhances our understanding of its classificatory mechanisms, potentially contributing to the development of more transparent and interpretable models across various domains of medical image analysis.

2 Discussion

This study introduces not only a novel model for haematological cell classification but, more crucially, a fundamental modelling approach and a principled evaluative framework. Both our approach and evaluative framework are grounded in the recognition of the inherent complexity of the target system and the constraints of applicable investigational and data regimes in medical imaging.

The characteristics of haematological cell classification mandate generative modelling, either as a preliminary to discriminative modelling or combined, as in our generative classifier, CytoDiffusion. This necessity arises from the fundamental inadequacy of learning a decision boundary in isolation. Such an approach will always be insufficient where the underlying distributions are as complex as those encountered in haematological cell morphology. Generative modelling, by contrast, can capture the full richness of these complex distributions.

Our empirical results manifest the failures of discriminative models, even state-of-the-art architectures trained on large-scale datasets, when subjected to an ecologically valid evaluative framework. This underscores the critical importance of assessing performance within this broader, more realistic context.

CytoDiffusion demonstrates substantial improvements over existing methods, without relying on careful hyperparameter tuning or data-specific architectural refinements. Importantly, these results likely represent a lower bound on potential performance, rather than a ceiling, highlighting the promise of this approach for further refinement and optimisation.

A key strength of our methodology is its recognition that the objective in medical imaging tasks like haematological cell classification is to achieve superhuman performance. This is attainable only by eliciting structure in the data that transcends expert labelling. While we have not fully exploited the representation learning capabilities of generative models in this work, there is significant potential for further advances, possibly through the use of generative modelling architectures with compact latents. Notably, CytoDiffusion’s confidence measure already demonstrates superhuman metacognitive capabilities, offering a more nuanced and reliable assessment of uncertainty than human experts.

Generative models also enable the assurance of equity in medical diagnostics. Although not implemented in this study, conditioning on minority characteristics would allow for legibility of differences in the model’s perception across diverse demographic groups. This capability is crucial for both detecting potential biases and enabling targeted remedial actions, ensuring fair and equitable application of AI in healthcare.

Our approach is not without limitations. The inference process of our CytoDiffusion is computationally expensive, scaling with the number of classes. However, this is less problematic in the medical domain, where datasets typically

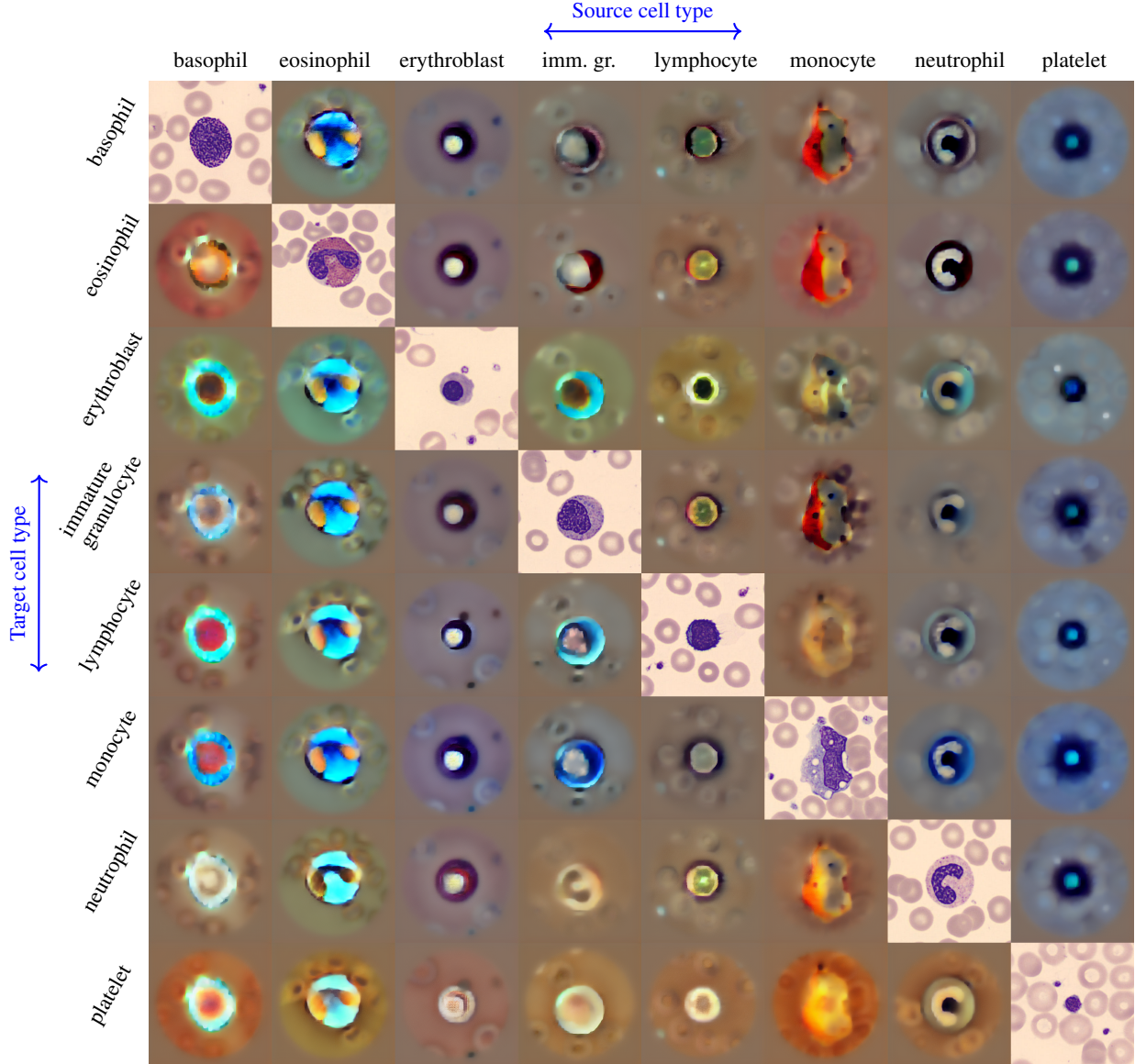


Figure 6: Counterfactual heatmaps for cell type transitions in the PBC dataset. The diagonal shows original images of each cell type, serving as the source. Each off-diagonal element in the same column represents a counterfactual heatmap (\mathbf{H}_c) showing the transition from the diagonal element (source) to the cell type of that row (target). Darker areas in the heatmaps indicate features to be added, whilst lighter areas suggest features to be removed to achieve the target cell type.

have far fewer classes than general image classification tasks like ImageNet. Moreover, CytoDiffusion’s adaptive allocation of computing resources, dedicating more effort to challenging images, makes it more effective.

In conclusion, this work establishes a new paradigm for medical image analysis, particularly in haematology. By embracing the inherent complexities of biological systems and the limitations of current data regimes, our generative approach with CytoDiffusion and comprehensive evaluation framework pave the way for more robust, interpretable, and equitable AI systems in healthcare. Future work should focus on refining these methods, exploring their applicability to other medical imaging domains, and further enhancing their computational efficiency without compromising performance.

3 Methods

3.1 Latent Diffusion Models

Generative models have seen significant advancements in recent years, with diffusion models emerging as a leading approach for creating high-quality data samples [47, 48, 49, 50, 51]. These models draw inspiration from thermodynamic diffusion processes [52] and have demonstrated impressive results in various tasks, such as image generation, inpainting, and super-resolution [53, 47, 54, 55, 56].

Diffusion models operate on the principle of defining a forward diffusion process, which gradually adds noise to the data, converting it into a noise-like distribution. The model then learns a reverse process to denoise the data, effectively reconstructing the original data distribution [52, 49].

In latent diffusion models, data \mathbf{x} is first encoded into a latent space using an encoder, typically a Variational Autoencoder (VAE), resulting in latent variables $\mathbf{z} = \mathcal{E}(\mathbf{x})$ with $\mathbf{z} \sim q(\mathbf{z})$ [57, 47, 58]. The forward and reverse diffusion processes are subsequently applied to these latent variables.

3.1.1 Forward Diffusion Process

The forward diffusion process is formulated as a Markov chain, wherein Gaussian noise is incrementally added to the latent variables over T steps. Let \mathbf{z}_0 denote a variable from the encoded (latent) data distribution. The forward process generates a sequence of latent variables $\mathbf{z}_1, \mathbf{z}_2, \dots, \mathbf{z}_T$ by successively introducing Gaussian noise, with distributions given by

$$q(\mathbf{z}_t | \mathbf{z}_{t-1}) = \mathcal{N}(\mathbf{z}_t; \sqrt{\alpha_t} \mathbf{z}_{t-1}, (1 - \alpha_t) \mathbf{I}), \quad (1)$$

where $\alpha_t \in (0, 1)$ gives the variance schedule [52]. The marginal distribution of \mathbf{z}_t given \mathbf{z}_0 is

$$q(\mathbf{z}_t | \mathbf{z}_0) = \mathcal{N}(\mathbf{z}_t; \sqrt{\bar{\alpha}_t} \mathbf{z}_0, (1 - \bar{\alpha}_t) \mathbf{I}), \quad (2)$$

with $\bar{\alpha}_t = \prod_{s=1}^t \alpha_s$. We will also write $\mathbf{z}_t = \sqrt{\bar{\alpha}_t} \mathbf{z}_0 + \sqrt{1 - \bar{\alpha}_t} \boldsymbol{\epsilon}$, where $\boldsymbol{\epsilon} \sim \mathcal{N}(0, \mathbf{I})$.

3.1.2 Reverse Diffusion Process

The reverse diffusion process seeks to reconstruct the latent variable by reversing the forward process. This process is parameterised by a learnable set of parameters θ , and is conditioned on some context c . We take it to be

$$p_\theta(\mathbf{z}_{t-1} | \mathbf{z}_t, c) = \mathcal{N}(\mathbf{z}_{t-1}; \boldsymbol{\mu}_\theta(\mathbf{z}_t, t, c), (1 - \alpha_t) \mathbf{I}), \quad (3)$$

where the mean $\boldsymbol{\mu}_\theta(\mathbf{z}_t, t, c)$ is given by

$$\boldsymbol{\mu}_\theta(\mathbf{z}_t, t, c) = \frac{1}{\sqrt{\alpha_t}} \left(\mathbf{z}_t - \frac{1 - \alpha_t}{\sqrt{1 - \bar{\alpha}_t}} \boldsymbol{\epsilon}_\theta(\mathbf{z}_t, t, c) \right), \quad (4)$$

and where $\boldsymbol{\epsilon}_\theta(\mathbf{z}_t, t, c)$ is learned to approximate $\boldsymbol{\epsilon}$ [49].

The training objective for diffusion models is based on the variational lower bound (VLB) of the negative log-likelihood of the data. However, it was shown in [49] that a simpler objective could be used, which measures the difference between the added noise and the noise predicted by the model:

$$\mathcal{L}_{\text{diffusion}} = \mathbb{E}_{\boldsymbol{\epsilon}, t} \left[w_t \|\boldsymbol{\epsilon} - \boldsymbol{\epsilon}_\theta(\mathbf{z}_t, t, c)\|_2^2 \right], \quad (5)$$

where $\boldsymbol{\epsilon} \sim \mathcal{N}(0, \mathbf{I})$, and $t \sim \mathcal{U}[1, T]$ [49]. In our experiments, we use this objective, taking $w_t = \min\{\frac{5}{\text{SNR}(t)}, 1\}$ [59].

3.2 Diffusion Classifiers

Recent studies have shown that diffusion models can also be utilised as classifiers [18, 19, 20, 17]. Given an input image \mathbf{x} , we want to predict the most probable class \hat{c} . This can be formalised as finding the class \hat{c} that maximises the posterior probability $p(c = c_k | \mathbf{x})$. Using Bayes' theorem, this is equivalent to

$$\hat{c} = \arg \max_{c_k} p(c = c_k | \mathbf{x}) = \arg \max_{c_k} p(\mathbf{x} | c = c_k) \cdot p(c = c_k) = \arg \max_{c_k} \log p(\mathbf{x} | c = c_k), \quad (6)$$

assuming a uniform prior over the classes, $p(c = c_k) = \frac{1}{K}$, where K is the number of classes.

As we do not have direct access to the (negative) log likelihood, we use our loss function to approximate it instead, and therefore take

$$\hat{c} = \arg \min_c \mathbb{E}_{\epsilon, t} \left[w_t \|\epsilon - \epsilon_\theta(z_t, t, c)\|_2^2 \right], \quad (7)$$

with the weight w_t as described below. To achieve this, we randomly pick a time step t and noise tensor ϵ and calculate the error

$$\|\epsilon - \epsilon_\theta(z_t, t, c)\|_2^2, \quad (8)$$

for all class labels c . These error values are then normalised using an appropriate weighting function. This normalisation aligns the errors for different t and ϵ to a common scale. Our empirical tests showed that the most effective weighting function was the reciprocal of a fourth-degree polynomial fitted to the median of the standard deviation of the squared errors. Further details on the weighting functions tested are available in the supplementary material A. After normalisation, the results are stored. The process then repeats with newly sampled values of t and ϵ . For an intuitive explanation of how our model makes its predictions, we refer to Figure 10 in supplementary material.

Using a procedure similar to [19], we repeatedly gather new sets of errors for each candidate class. Classes that are less likely to be the lowest-error (and thus predicted) class as more samples are taken are progressively eliminated. This is achieved using a paired Student’s t -test, which compares the errors across classes. However, given that the errors do not perfectly follow the standard assumptions of a Student’s t -test, we employ a small p-value of 2×10^{-3} to ensure robustness. This iterative procedure continues until there is only one class left or a maximum number of iterations is reached. Unless stated otherwise, we use a minimum of 20 iterations and a maximum of 2000 iterations in our experiments.

3.3 General Training Setup

Unless otherwise specified, we employed the following training configuration for all experiments. We used Stable Diffusion 1.5 [47] as our base model. For class conditioning, we bypassed the tokeniser and text encoder, directly feeding the model with one-hot encoded vectors for each class, replicated vertically and padded horizontally to match the expected matrix of 77×768 dimensions. We utilised a batch size of 10, a learning rate of 10^{-5} with linear warmup over 1000 steps, and trained on an A100-80GB GPU.

We applied various data augmentations, including random diagonal flips, 360-degree rotation, colour jitter (brightness=0.25, contrast=0.25, saturation=0.25, hue=0.125), and mixup [60] ($\alpha = 0.3$) applied to the conditioning instead of the target. Additionally, we employed `torchvision.transforms.RandAugment` with default parameters. We used an AdamW optimiser ($\beta_1 = 0.9$, $\beta_2 = 0.999$, $\epsilon = 10^{-8}$, weight decay 0.01), mixed precision training (fp16), and an exponential moving average of 0.9999. All images were resized to 360×360 pixels.

During inference, we applied the same data augmentations used in training, excluding `torchvision.transforms.RandAugment` and mixup. Leveraging the fact that white blood cells are typically centred in the image, and to mitigate the effects of augmentations that corrupt the outer parts of the image, we calculated the inference error only for pixels within a radius of 20 from the centre of the image in our latent space, which has dimensions of $45 \times 45 \times 4$.

For comparisons with EfficientNetV2-M [45] and ViT-B/16 [44], pre-trained on ImageNet [61], we maintained consistent data augmentation techniques and optimiser settings. However, to accommodate the ViT-B/16 model’s input size requirements of 384×384 pixels, we first resized the images to match our diffusion model’s input size and then further resized them to 384×384 pixels. For these comparison models, we used a batch size of 16, a learning rate of 10^{-4} , and trained for 50 epochs. The model checkpoint with the highest validation accuracy was selected for testing.

3.4 Datasets

We utilised multiple datasets, including publicly available ones and a custom dataset, to develop and evaluate our diffusion classifier for haematological cell classification. Our custom dataset, which we will release publicly as soon as we have obtained the necessary ethics approvals, consists of 559,808 single cell images from 2,904 blood smear slides obtained from Addenbrooke’s Hospital in Cambridge, with a labelled subset of 5,000 images across 10 classes. Importantly, all images were anonymised before we received them, ensuring patient privacy and ethical compliance. These images were created using Cellavision, a specialised imaging technology for cellular analysis. Notably, we included an artefact class in our dataset, addressing a critical challenge in clinical applications. Blood smear slides often contain artefacts that can be mistaken for cells by deep learning-based cell detection models. By explicitly modelling these artefacts, our dataset aims to enhance clinical applicability.

A distinctive feature of our dataset is the inclusion of labeller confidence scores, an attribute rarely found in existing datasets. This addition provides valuable information for various analyses beyond simple correlations. For instance, it

enables in-depth comparisons between model and human expert performance, particularly in how certainty relates to accuracy. Researchers can investigate the patterns of confidence exhibited by models and human experts across different cases, and identify specific scenarios where models might demonstrate different certainty-accuracy relationships compared to human experts. Such analyses offer insights into the strengths and limitations of both AI models and human experts in haematological cell classification. For a more detailed analysis of how labellers' confidence levels correlate with each other see the supplementary material, Figure 9. Table 3 summarises the datasets used in our study, highlighting the unique attributes of our custom dataset.

Our custom dataset's labelling process involved six haematology experts with $\{34, 25, 15, 12, 6, 5\}$ years of experience in blood microscopy, respectively. Each expert labelled 1,000 images, including 200 common images for inter-rater reliability assessment. Experts assigned one of ten classes (basophil, blast, lymphocyte, monocyte, neutrophil, erythroblast, eosinophil, immature granulocyte, platelet, or artefact) and indicated their confidence level (High, Moderate, Low, or No Confidence) for each prediction. For images labelled by multiple experts, we used a majority vote to determine the final label. In case of a tie, the label provided by the expert with the longest experience in blood microscopy was used.

To optimise the use of our expert labellers' time whilst also attempting to identify potential labelling errors, we employed a strategic review process. We trained our model using a 3-fold cross-validation approach, ensuring all images except the 200 common ones were used in the test set once. We then applied each model to its respective test set, effectively covering the entire dataset (excluding the 200 common images) with predictions from models that had not seen those images during training. Images for which the model's prediction did not agree with the original label were selected for review by two expert haematologists who had not previously labelled these specific images. This review process resulted in 816 images being evaluated by the two additional experts, of which 407 images had their class labels changed.

To implement this strategy, we continued the pretraining of a Stable Diffusion 1.5 model [47] using a combination of ImageNet [61] and our unlabelled blood image dataset, with equal selection probability. The inclusion of ImageNet alongside our unlabelled blood images was crucial to prevent the model from unlearning its conditioning capabilities. Due to the large number of classes in ImageNet, which precluded the use of one-hot encoding, we employed binary encoded vectors for each class.

For this initial phase, we employed a batch size of 64 and trained on an A100-80GB GPU for 76,000 steps. We refer to the model resulting from this first phase as our base model. In the second phase, we used our base model to train our 3-fold cross-validation models for 45,000 steps each.

Table 3: Summary of the datasets used in our experiments.

Dataset	# Images	# Classes	Labeller Confidence	Artifacts
Raabbin-WBC [62]	17,965	5	✗	✗
LISC [63]	257	5	✗	✗
PBC [22]	17,092	8	✗	✗
Bodzas [43]	16,027	9	✗	✗
Ours	5,000	$9 + 1^*$	✓	✓

* 9 regular classes of blood cells plus 1 artefact class.

3.5 Turing Test

To assess the quality and authenticity of our fine-tuned diffusion model's synthetic blood cell images, we conducted a Turing test with expert haematologists. This evaluation was designed to determine whether the model could effectively capture the underlying distribution of blood cell images across various cell types, a capability that traditional discriminative models are not inherently required to possess. Additionally, we sought to assess the accuracy of the generated cell types.

We fine-tuned CytoDiffusion on the combined PBC and Bodzas datasets, with all images resized to 512×512 pixels. From this combined dataset, we randomly selected 1,400 images for validation, with the remaining images allocated to the training set. The model was trained for 44,000 steps, employing a limited augmentation strategy that included only random vertical and horizontal flips.

Following the training phase, we generated a set of 144 synthetic images spanning all the classes using 50 inference steps. Each image was conditioned on one of nine blood cell types: basophil, blast, lymphocyte, monocyte, neutrophil, erythroblast, eosinophil, immature granulocyte, and platelet. For the Bodzas dataset, we merged the neutrophil segment and neutrophil band classes into a single neutrophil class and created a blast class, which comprised both lymphoblasts

and myeloblasts. To create a balanced dataset for the Turing test, we randomly selected an equivalent set of 144 real images from our validation dataset, resulting in a total pool of 288 images.

Ten haematology specialists from our research group, with $\{34, 28, 25, 15, 10, 9, 6, 5, 5, 0\}$ years of experience in blood microscopy, participated in the Turing test. Participants were informed that half of the images presented to them would be real images from our dataset, while the other half would be synthetic images generated by our model. Each specialist was presented with the 288 images in a randomised order and asked to perform two tasks: (1) Distinguish between synthetically generated and real images and (2) classify each image into one of the nine designated blood cell types.

3.6 In-Domain Performance

To establish a baseline for our diffusion-based classifier, CytoDiffusion, we evaluated its performance on standard in-domain classification tasks using three datasets: our custom dataset, Raabin-WBC, and PBC. For the Raabin-WBC dataset, we utilised the predefined Train split (90% for training, 10% for validation) and tested on the predefined TestA dataset. For the PBC dataset, we employed an 80–10–10 split for train–validation–test.

For our custom dataset, we employed a cross-validation approach. We divided the dataset into four folds and fine-tuned four separate models, enabling us to test on the full dataset. For each fold used in training, we further split the data into 80% for training and 20% for validation and we trained each model for 60,000 iterations.

For the Raabin-WBC and PBC datasets, we trained our model for 72,000 steps. For comparison, we also trained and evaluated EfficientNetV2-M and ViT-B/16 models.

Given the significant class imbalances present in these datasets (Raabin-WBC TestA ranges from 89 to 2,660 images per class, our custom dataset from 103 to 1,425, and PBC from 1,199 to 3,314), we report both overall accuracy and balanced accuracy.

3.7 Uncertainty Measure

To assess the relationship between model performance and uncertainty, we employed psychometric function analysis. This approach allows us to quantify how closely our model’s uncertainty measure approximates that of an ideal observer, exhibiting purely aleatoric uncertainty.

We utilised the cross-validated models trained on our custom dataset, as described in Section 3.6. For quantifying the model’s uncertainty, we calculated the difference between the two classes with the smallest error, rescaled in the interval $[0, 1]$. To establish a measure of labeller uncertainty, we mapped the confidence levels provided by our expert haematologists to numerical values: 1.0 for High Confidence, 2/3 for Moderate Confidence, 1/3 for Low Confidence, and 0.0 for No Confidence. For images assessed by multiple labellers, we averaged their uncertainty scores.

Psychometric functions describe the relation between the performance of an observer and a (typically scalar) property of the observed. The performance of interest is usually detection or classification, expressed as a function of signal strength on a monotonically increasing scale. Since an ideal model is as confident as the data allows, exhibiting purely aleatoric uncertainty, we can quantify the proximity of a model to that ideal by fitting a psychometric function with model confidence as the index of signal strength. A good measure of uncertainty should conform closely to an ideal observer, yielding a sigmoid curve rising from a chance guess rate, γ , where uncertainty is maximal, to a lapse rate λ , where uncertainty is minimal and any errors are not explicable by insufficient information.

The “threshold” of the function (m)—an arbitrarily chosen point—and its slope or width (w) are ordinarily measures of performance relative to a ground truth signal strength. Since there is no ground truth here, the goodness of fit of the function to the data, and the separability of different observers are our measures of the quality of the uncertainty. The psychometric function is then defined as

$$\psi(x; m, w, \gamma, \lambda) = \lambda + (1 - \lambda - \gamma)S(x; m, w), \quad (9)$$

where S is a sigmoid, here chosen as the logistic, scaled in the interval $[0, 1]$. We use Bayesian inference, implemented in psignifit (<https://github.com/wichmann-lab/psignifit> under MATLAB 2022b), to obtain parameter estimates, with priors informed by the psychophysical literature [42]. For the threshold, we use a uniform prior over the range of the data with a cosine fall off to 0 over half the range of the data on either side of the maximum and the minimum, expressing a belief that the threshold is located with equal probability within the sampled range and may be up to 50% of the spread of the data outside that range with decreasing probability. For the width, we use a uniform prior between two times the minimal distance of two tested stimulus levels and the range of the stimulus levels with cosine fall offs to 0 at the minimal difference of two stimulus levels and at 3 times the range of the tested stimulus. For γ , we fix the parameter at 1/10, reflecting the 10 possible classes, and for λ we use a beta-distribution with parameters (1,10). We report the threshold and width estimated parameters, and their posterior distributions, citing 95% credibility intervals.

Functions were fitted to CytoDiffusion performance with its uncertainty, with data from the entire test set; to individual expert performance with consensus expert uncertainty, with data from 200 cases for which consensus uncertainty was available; and to individual expert performance with CytoDiffusion model uncertainty, again with data from 200 cases for which consensus uncertainty was available. To provide sufficient support for each evaluated performance level, uncertainties were discretized into 25 bins for the CytoDiffusion function (where the full test set was available), and 12 bins for the expert functions (where 200 cases were available).

3.8 Anomaly Detection

To evaluate our model’s capability in detecting anomalous cell types, we designed an experiment that simulates real-world scenarios where rare or previously unseen cell types might appear in clinical samples. This approach involved excluding specific abnormal cell classes during training and assessing the model’s ability to identify these classes during testing.

We utilised two datasets for this experiment: the Bodzas dataset and the PBC dataset. For the Bodzas dataset, we merged the neutrophil segment and neutrophil band classes into a single neutrophil class and excluded the blasts class, which comprised both lymphoblasts and myeloblasts (5,036 images in total). From the PBC dataset, we excluded the erythroblast class (1,513 images). The data was split into 70% training, 10% validation, and 20% test sets, with all abnormal cells (blasts and erythroblasts) moved to their respective test sets.

We fine-tuned two diffusion models, one for each dataset, training each for 140,000 steps on an NVIDIA RTX A5000 GPU. For comparison, we also fine-tuned a Vision Transformer (ViT-B/16) model [44] for each dataset.

We used the uncertainty described in Section 1.3. To visualise each model’s ability to distinguish between normal and abnormal cells, we generated KDE curves of the confidence differences for both groups. To quantify this ability, we calculated the AUC for each model and dataset.

3.9 Domain Shift

To evaluate our model’s robustness under domain shift conditions, we leveraged the Raabin-WBC dataset [62] and the LISC dataset [63], following methodologies outlined in previous studies [31, 30]. We utilised the predefined Train split for training (90%) and validation (10%), and the TestB split as one of our test sets. The TestB split was created using a different microscope and camera type compared to the training and validation set, introducing a domain shift. Additionally, we employed the LISC dataset as a second test set, which was created using different microscope and camera types, as well as a different staining method, further increasing the domain shift challenge. To maintain consistency with previous studies [31, 30] and accommodate the lower resolution of LISC images, we resized all images to 224×224 pixels. We used a batch size of 32 and trained for 22,000 steps on an NVIDIA RTX A5000 GPU.

For comparison, we also fine-tuned and tested EfficientNetV2-M and ViT-B/16. To ensure reliable performance evaluation, we repeated the training and evaluation process five times for each of the models (our diffusion-based model, EfficientNetV2-M, and ViT-B/16).

3.10 Efficiency

To assess the efficiency of our model in learning from a small number of images per class, we designed an experiment using the PBC dataset [22]. We randomly selected 250 images per class for the training set, 836 images per class for the test set, and the remaining images for the validation set. From the training set, we randomly sampled subsets of 10, 20, 50, or 150 images per class to simulate low-data scenarios.

We trained CytoDiffusion on an NVIDIA RTX A5000 GPU. For subsets of 10, 20, 50, and 150 images per class, we trained for 20,000, 40,000, 100,000, and 240,000 steps respectively, saving checkpoints every 1000, 3000, 7000, and 20000 steps. For each subset, we selected the checkpoint with the highest validation accuracy for testing.

For comparison, we also trained and evaluated EfficientNetV2-M and ViT-B/16 models using the same data subsets. To account for variability in the subsampling and initialisations, we repeated each experiment five times. This involved resampling the specified number of images per class (10, 20, 50, and 150) and retraining all models for each repetition.

3.11 Explainability

One of the integral aspects of CytoDiffusion’s utility in clinical settings is its ability to provide explainable predictions. To achieve this, we employ a counterfactual heatmap approach, which elucidates what changes would be necessary

for an image to be classified under a different specified class. This method is particularly beneficial for understanding model decisions in complex medical imaging tasks such as the classification of blood cell types.

The process begins by calculating the difference between the original noise tensor, ϵ , and the noise tensor predicted by the model for each class condition c . This difference is recorded for all iterations, and the mean error tensor for each condition c is computed as

$$\Delta_c = \frac{1}{N} \sum_{n=1}^N (\epsilon_n - \epsilon_\theta(\mathbf{z}_{t_n}, t_n, c)) , \quad (10)$$

where N is the number of iterations.

Subsequently, for each class condition c , we calculate the deviation from the condition with the minimum error, designated as $\Delta_{\hat{c}}$, where \hat{c} is the predicted class. The adjusted tensor, δ_c , is then

$$\delta_c = \Delta_c - \Delta_{\hat{c}} . \quad (11)$$

Finally, these adjusted tensors δ_c are decoded back to the pixel space using the VAE decoder to obtain the counterfactual heatmaps

$$\mathbf{H}_c = \mathcal{D}(\delta_c) , \quad (12)$$

where \mathcal{D} denotes the VAE decoder, and \mathbf{H}_c represents the heatmap for condition c . These heatmaps visually represent modifications that would shift the image classification from the predicted class to the target class c , thereby providing a powerful tool for explaining and validating model predictions.

Consortia

The members of the BloodCounts! consortium are: Martijn Schut, Folkert Asselbergs, Sujoy Kar, Suthesh Sivapalaratnam, Sophie Williams, Mickey Koh, Yvonne Henskens, Bart de Wit, Umberto D'Alessandro, Bubacarr Bah, Ousman Secka, Parashkev Nachev, Rajeev Gupta, Sara Trompeter, Nancy Boeckx, Christine van Laer, Gordon A. Awandare, Kwabena Sarpong, Lucas Amenga-Etego, Mathie Leers, Mirelle Huijskens, Samuel McDermott, Willem H. Ouwehand, James Rudd, Carola-Bibiane Schönlieb, Nicholas Gleadall and Michael Roberts.

References

- [1] Barbara J Bain. *Blood cells: a practical guide*. John Wiley & Sons, 2021.
- [2] Bain Barbara J. Diagnosis from the blood smear. *New England Journal of Medicine*, 353(5):498–507, 2005.
- [3] Alexander Kratz, Szu-hee Lee, Gina Zini, Jurgen A. Riedl, Mina Hur, Sam Machin, and the International Council for Standardization in Haematology. Digital morphology analyzers in hematology: Icsh review and recommendations. *International Journal of Laboratory Hematology*, 41(4):437–447, 2019.
- [4] Mauro Buttarello and Mario Plebani. Automated blood cell counts: State of the art. *American Journal of Clinical Pathology*, 130(1):104–116, July 2008.
- [5] Gert-Jan van de Geijn, Vincent van Rees, Natasja van Pul-Bom, Erwin Birnie, Hans Janssen, Hans Pegels, Marlène Beunis, and Tjin Njo. Leukoflow: Multiparameter extended white blood cell differentiation for routine analysis by flow cytometry. *Cytometry Part A*, 79A(9):694–706, 2011.
- [6] G E Metter, B N Nathwani, J S Burke, C D Winberg, R B Mann, M Barcos, C R Kjeldsberg, C C Whitcomb, D O Dixon, and T P Miller. Morphological subclassification of follicular lymphoma: variability of diagnoses among hematopathologists, a collaborative study between the repository center and pathology panel for lymphoma clinical studies. *Journal of Clinical Oncology*, 3(1):25–38, January 1985.
- [7] Jee Seok Yoon, Kwanseok Oh, Yooseung Shin, Maciej A. Mazurowski, and Heung-Il Suk. Domain generalization for medical image analysis: A survey, 2024.
- [8] Pang Wei Koh, Shiori Sagawa, Henrik Marklund, Sang Michael Xie, Marvin Zhang, Akshay Balsubramani, Weihua Hu, Michihiro Yasunaga, Richard Lanas Phillips, Irena Gao, Tony Lee, Etienne David, Ian Stavness, Wei Guo, Berton Earnshaw, Imran Haque, Sara M. Beery, Jure Leskovec, Anshul Kundaje, Emma Pierson, Sergey Levine, Chelsea Finn, and Percy Liang. Wilds: A benchmark of in-the-wild distribution shifts. In *Proceedings of the 38th International Conference on Machine Learning*, page 5637–5664. PMLR, July 2021.
- [9] Amirhossein Kazerouni, Ehsan Khodapanah Aghdam, Moein Heidari, Reza Azad, Mohsen Fayyaz, Ilker Haci-haliloglu, and Dorit Merhof. Diffusion models in medical imaging: A comprehensive survey. *Medical Image Analysis*, 88:102846, August 2023.
- [10] Edmon Begoli, Tanmoy Bhattacharya, and Dimitri Kusnezov. The need for uncertainty quantification in machine-assisted medical decision making. *Nature Machine Intelligence*, 1(1):20–23, January 2019.
- [11] Luke Oakden-Rayner, Jared Dunnmon, Gustavo Carneiro, and Christopher Re. Hidden stratification causes clinically meaningful failures in machine learning for medical imaging. In *Proceedings of the ACM Conference on Health, Inference, and Learning*, CHIL ’20, page 151–159, New York, NY, USA, April 2020. Association for Computing Machinery.
- [12] Andreas Holzinger, Georg Langs, Helmut Denk, Kurt Zatloukal, and Heimo Müller. Causability and explainability of artificial intelligence in medicine. *Wiley Interdisciplinary Reviews. Data Mining and Knowledge Discovery*, 9(4):e1312, 2019.
- [13] Cynthia Rudin. Stop explaining black box machine learning models for high stakes decisions and use interpretable models instead. *Nature Machine Intelligence*, 1(5):206–215, May 2019.
- [14] Rabia Asghar, Sanjay Kumar, Paul Hynds, and Arslan Shaukat. Classification of white blood cells using machine and deep learning models: A systematic review, 2023.
- [15] Rabia Asghar, Sanjay Kumar, and Paul Hynds. Automatic classification of 10 blood cell subtypes using transfer learning via pre-trained convolutional neural networks. *Informatics in Medicine Unlocked*, page 101542, June 2024.
- [16] Hüseyin Firat. Classification of microscopic peripheral blood cell images using multibranch lightweight cnn-based model. *Neural Computing and Applications*, 36(4):1599–1620, February 2024.
- [17] Alexander Cong Li, Ananya Kumar, and Deepak Pathak. Generative classifiers avoid shortcut solutions. In *ICML 2024 Workshop on Structured Probabilistic Inference & Generative Modeling*, 2024.
- [18] Huanran Chen, Yinpeng Dong, Zhengyi Wang, Xiao Yang, Chengqi Duan, Hang Su, and Jun Zhu. Robust classification via a single diffusion model. *arXiv preprint arXiv:2305.15241*, 2023.
- [19] Kevin Clark and Priyank Jaini. Text-to-image diffusion models are zero shot classifiers. *Advances in Neural Information Processing Systems*, 36, 2024.
- [20] Alexander C Li, Mihir Prabhudesai, Shivam Duggal, Ellis Brown, and Deepak Pathak. Your diffusion model is secretly a zero-shot classifier. In *Proceedings of the IEEE/CVF International Conference on Computer Vision*, pages 2206–2217, 2023.

[21] Zahra Mousavi Kouzehkanan, Sepehr Saghari, Sajad Tavakoli, Peyman Rostami, Mohammadjavad Abaszadeh, Farzaneh Mirzadeh, Esmaeil Shahabi Satlsar, Maryam Gheidishahran, Fatemeh Gorgi, Saeed Mohammadi, and Reshad Hosseini. A large dataset of white blood cells containing cell locations and types, along with segmented nuclei and cytoplasm. *Scientific Reports*, 12(1):1123, January 2022.

[22] Andrea Acevedo, Anna Merino, Santiago Alférez, Ángel Molina, Laura Boldú, and José Rodellar. A dataset of microscopic peripheral blood cell images for development of automatic recognition systems. *Data in Brief*, 30:105474, June 2020.

[23] Ruitao Zhang, Xueying Han, Zhengyang Lei, Chenyao Jiang, Ijaz Gul, Qiuyue Hu, Shiyao Zhai, Hong Liu, Lijin Lian, Ying Liu, Yongbing Zhang, Yuhan Dong, Can Yang Zhang, Tsz Kwan Lam, Yuxing Han, Dongmei Yu, Jin Zhou, and Peiwu Qin. Remnet: A deep learning model assists car-t therapy for leukemia. *Computers in Biology and Medicine*, 150:106084, November 2022.

[24] Fei Long, Jing-Jie Peng, Weitao Song, Xiaobo Xia, and Jun Sang. Bloodcaps: A capsule network based model for the multiclassification of human peripheral blood cells. *Computer Methods and Programs in Biomedicine*, 202:105972, April 2021.

[25] Rufus Rubin, S. M. Anzar, Alavikunhu Panthakkan, and Wathiq Mansoor. Transforming healthcare: Raabin white blood cell classification with deep vision transformer. In *2023 6th International Conference on Signal Processing and Information Security, ICSPIS 2023*, page 212–217. Institute of Electrical and Electronics Engineers Inc., 2023.

[26] Sajad Tavakoli, Ali Ghaffari, Zahra Mousavi Kouzehkanan, and Reshad Hosseini. New segmentation and feature extraction algorithm for classification of white blood cells in peripheral smear images. *Scientific Reports*, 11(1):19428, September 2021.

[27] Hua Chen, Juan Liu, Chunbing Hua, Jing Feng, Baochuan Pang, Dehua Cao, and Cheng Li. Accurate classification of white blood cells by coupling pre-trained resnet and densenet with scam mechanism. *BMC Bioinformatics*, 23:282, July 2022.

[28] Jiang L, Tang C, and Zhou H. White blood cell classification via a discriminative region detection assisted feature aggregation network. *Biomedical optics express*, 13(10), September 2022.

[29] Eduardo Rivas-Posada and Mario I. Chacon-Murguia. Automatic base-model selection for white blood cell image classification using meta-learning. *Computers in Biology and Medicine*, 163:107200, September 2023.

[30] Satoshi Tsutsui, Zhengyang Su, and Bihang Wen. Benchmarking white blood cell classification under domain shift. In *ICASSP 2023 - 2023 IEEE International Conference on Acoustics, Speech and Signal Processing (ICASSP)*, page 1–5, June 2023.

[31] Chongchong Li and Yuting Liu. Improved generalization of white blood cell classification by learnable illumination intensity invariant layer. *IEEE Signal Processing Letters*, 31:176–180, 2024.

[32] Ferhat Ucar. Deep learning approach to cell classification in human peripheral blood. *2020 5th International Conference on Computer Science and Engineering (UBMK)*, page 383–387, September 2020.

[33] Priyanka Rastogi, Kavita Khanna, and Vijendra Singh. Leufeatx: Deep learning-based feature extractor for the diagnosis of acute leukemia from microscopic images of peripheral blood smear. *Computers in Biology and Medicine*, 142:105236, March 2022.

[34] Mohamad Abou Ali, Fadi Dornaika, and Ignacio Arganda-Carreras. Blood cell revolution: Unveiling 11 distinct types with ‘naturalize’ augmentation. *Algorithms*, 16(12):562, December 2023.

[35] Omid Nejati Manzari, Hamid Ahmadabadi, Hossein Kashiani, Shahriar B. Shokouhi, and Ahmad Ayatollahi. Medvit: A robust vision transformer for generalized medical image classification. *Computers in Biology and Medicine*, 157:106791, May 2023. arXiv:2302.09462 [cs].

[36] Faris Almalik, Naif Alkhunaizi, Ibrahim Almakky, and Karthik Nandakumar. Fesvibs: Federated split learning of vision transformer with block sampling. In *International Conference on Medical Image Computing and Computer-Assisted Intervention*, pages 350–360. Springer, 2023.

[37] Sudhakar Tummala and Anil K. Suresh. Few-shot learning using explainable siamese twin network for the automated classification of blood cells. *Medical & Biological Engineering & Computing*, 61(6):1549–1563, June 2023.

[38] Alex Kendall and Yarin Gal. What uncertainties do we need in bayesian deep learning for computer vision? *Advances in neural information processing systems*, 30, 2017.

[39] Yaniv Ovadia, Emily Fertig, Jie Ren, Zachary Nado, D. Sculley, Sebastian Nowozin, Joshua Dillon, Balaji Lakshminarayanan, and Jasper Snoek. Can you trust your model’s uncertainty? evaluating predictive uncertainty under dataset shift. In *Advances in Neural Information Processing Systems*, volume 32. Curran Associates, Inc., 2019.

[40] George A. Gescheider. *Psychophysics: The Fundamentals*. Psychology Press, New York, 3 edition, May 1997.

[41] Malte Kuss, Frank Jäkel, and Felix A. Wichmann. Bayesian inference for psychometric functions. *Journal of Vision*, 5(5):8, May 2005.

[42] Heiko H Schütt, Stefan Harmeling, Jakob H Macke, and Felix A Wichmann. Painfree and accurate bayesian estimation of psychometric functions for (potentially) overdispersed data. *Vision research*, 122:105–123, 2016.

[43] Alexandra Bodzas, Pavel Kodytek, and Jan Zidek. A high-resolution large-scale dataset of pathological and normal white blood cells. *Scientific Data*, 10(11):466, July 2023.

[44] Alexey Dosovitskiy, Lucas Beyer, Alexander Kolesnikov, Dirk Weissenborn, Xiaohua Zhai, Thomas Unterthiner, Mostafa Dehghani, Matthias Minderer, Georg Heigold, Sylvain Gelly, Jakob Uszkoreit, and Neil Houlsby. An image is worth 16x16 words: Transformers for image recognition at scale, 2021.

[45] Mingxing Tan and Quoc Le. Efficientnetv2: Smaller models and faster training. In *International conference on machine learning*, pages 10096–10106. PMLR, 2021.

[46] Helene F. Rosenberg, Kimberly D. Dyer, and Paul S. Foster. Eosinophils: changing perspectives in health and disease. *Nature Reviews Immunology*, 13(1):9–22, January 2013.

[47] Robin Rombach, Andreas Blattmann, Dominik Lorenz, Patrick Esser, and Björn Ommer. High-resolution image synthesis with latent diffusion models. In *Proceedings of the IEEE/CVF conference on computer vision and pattern recognition*, pages 10684–10695, 2022.

[48] Minshuo Chen, Song Mei, Jianqing Fan, and Mengdi Wang. An overview of diffusion models: Applications, guided generation, statistical rates and optimization. *arXiv preprint arXiv:2404.07771*, 2024.

[49] Jonathan Ho, Ajay Jain, and Pieter Abbeel. Denoising diffusion probabilistic models. *Advances in neural information processing systems*, 33:6840–6851, 2020.

[50] Yang Song, Jascha Sohl-Dickstein, Diederik P Kingma, Abhishek Kumar, Stefano Ermon, and Ben Poole. Score-based generative modeling through stochastic differential equations. *arXiv preprint arXiv:2011.13456*, 2020.

[51] Yang Song and Stefano Ermon. Improved techniques for training score-based generative models. In *Advances in Neural Information Processing Systems*, volume 33, page 12438–12448. Curran Associates, Inc., 2020.

[52] Jascha Sohl-Dickstein, Eric Weiss, Niru Maheswaranathan, and Surya Ganguli. Deep unsupervised learning using nonequilibrium thermodynamics. In *International conference on machine learning*, pages 2256–2265. PMLR, 2015.

[53] Chitwan Saharia, William Chan, Saurabh Saxena, Lala Li, Jay Whang, Emily L Denton, Kamyar Ghasemipour, Raphael Gontijo Lopes, Burcu Karagol Ayan, Tim Salimans, et al. Photorealistic text-to-image diffusion models with deep language understanding. *Advances in neural information processing systems*, 35:36479–36494, 2022.

[54] Chitwan Saharia, William Chan, Huiwen Chang, Chris Lee, Jonathan Ho, Tim Salimans, David Fleet, and Mohammad Norouzi. Palette: Image-to-image diffusion models. In *ACM SIGGRAPH 2022 conference proceedings*, pages 1–10, 2022.

[55] Andreas Lugmayr, Martin Danelljan, Andres Romero, Fisher Yu, Radu Timofte, and Luc Van Gool. Repaint: Inpainting using denoising diffusion probabilistic models. In *Proceedings of the IEEE/CVF conference on computer vision and pattern recognition*, pages 11461–11471, 2022.

[56] Chitwan Saharia, Jonathan Ho, William Chan, Tim Salimans, David J Fleet, and Mohammad Norouzi. Image super-resolution via iterative refinement. *IEEE transactions on pattern analysis and machine intelligence*, 45(4):4713–4726, 2022.

[57] Aaron Van Den Oord, Oriol Vinyals, et al. Neural discrete representation learning. *Advances in neural information processing systems*, 30, 2017.

[58] Diederik P Kingma and Max Welling. Auto-encoding variational bayes. *arXiv preprint arXiv:1312.6114*, 2013.

[59] Tiankai Hang, Shuyang Gu, Chen Li, Jianmin Bao, Dong Chen, Han Hu, Xin Geng, and Baining Guo. Efficient diffusion training via min-snri weighting strategy. In *Proceedings of the IEEE/CVF International Conference on Computer Vision*, pages 7441–7451, 2023.

- [60] Hongyi Zhang, Moustapha Cisse, Yann N Dauphin, and David Lopez-Paz. mixup: Beyond empirical risk minimization. *arXiv preprint arXiv:1710.09412*, 2017.
- [61] Jia Deng, Wei Dong, Richard Socher, Li-Jia Li, Kai Li, and Li Fei-Fei. Imagenet: A large-scale hierarchical image database. In *2009 IEEE Conference on Computer Vision and Pattern Recognition*, page 248–255, June 2009.
- [62] Zahra Mousavi Kouzehkanan, Sepehr Saghari, Sajad Tavakoli, Peyman Rostami, Mohammadjavad Abaszadeh, Farzaneh Mirzadeh, Esmaeil Shahabi Satlsar, Maryam Gheidishahran, Fatemeh Gorgi, Saeed Mohammadi, and Reshad Hosseini. A large dataset of white blood cells containing cell locations and types, along with segmented nuclei and cytoplasm. *Scientific Reports*, 12(11):1123, January 2022.
- [63] Seyed Hamid Rezatofighi and Hamid Soltanian-Zadeh. Automatic recognition of five types of white blood cells in peripheral blood. *Computerized Medical Imaging and Graphics*, 35(4):333–343, 2011.

Table 4: Accuracy results for different weighting strategies.

Weighting Strategy	Accuracy after 1000 trials	Mean Accuracy
Custom polynomial	0.9504	0.8805
Logistic regression	0.9458	0.8761
Normalised $\mathcal{N}(0, 1)$	0.9504	0.8743
Uniform	0.9371	0.8704
SNR	0.9371	0.8704
Ranking	0.9467	0.8689
$\exp(-5.5t)$	0.9287	0.8642

A Ablation Studies on Weighting Functions and Pruning Hyperparameters

We conducted extensive ablation studies on different weighting functions and pruning hyperparameters to optimise our model’s performance. Our investigations began with the ‘Heuristic’ and ‘Learned’ weighting functions described in [19]. The ‘Heuristic’ function takes the form $\exp(-kt)$, where t is between 0 and 1, and k was initially set to 6 or 7. The ‘Learned’ function involved dividing the time interval into 20 buckets and fitting a logistic regression function to a small portion of the data to learn the weights.

Our findings revealed that whilst the median error scaled exponentially with time (with $k = 5.5$ in our case, which performed better than 6 or 7), the standard deviation of the error did not follow this pattern. Instead, it formed a curve similar to a negative quadratic function. Given that our primary concern is relative differences rather than absolute values, we focused on this aspect. Consequently, we fitted a fourth-degree polynomial to the median of the standard deviation of the squared errors using data from the efficiency experiment with 20 images per class and used the reciprocal of this as our weighting function. The coefficients of our polynomial function are

$$f(t) = 0.927 + 9.837t - 4.684t^2 + 6.019t^3 - 9.340t^4, \quad (13)$$

and this weighting function was used consistently for all experiments presented in this paper. Empirically, this approach outperformed even the fitted ‘Learned’ logistic regression when using 240 images to train the logistic regression. Notably, our method generalised well, performing effectively on other datasets for which it was not specifically fitted.

We also explored alternative weighting functions. One approach involved calculating the error for all conditions c for one ϵ and t , normalising it to mean 0 and standard deviation 1, then drawing new ϵ and t , normalising to $\mathcal{N}(0, 1)$ etc. and taking the mean of all normalised errors. Another method ranked the errors, assigning a value of 1 to the lowest scoring error, 2 to the next lowest, and so on, before averaging across all trials. We also tested uniform weighting and the SNR weighting used for training: $\min\{\frac{5}{\text{SNR}(t)}, 1\}$.

To evaluate these weighting functions, we conducted ablation studies where we trained a model as described in Section 1.6 with 20 images per class. During inference, we used $\{1, 5, 10, 20, 50, 100, 250, 500, 1000\}$ trials per class without any pruning for each weighting function. Table 4 presents our results, showing the accuracy after 1000 trials and the mean accuracy across all trials. Our custom weighting function performed best, with the logistic regression and the normalised $\mathcal{N}(0, 1)$ approaches following closely behind.

We further investigated the impact of the p-value threshold for our pruning and the number of trials to conduct before initiating the Student’s t -test to determine if any class should be pruned. Figure 7 illustrates these results, showing the mean and standard deviation across all weighting functions combined.

The left panel of Figure 7 demonstrates that performance continues to improve with the number of trials per class, even beyond 1000 trials (no pruning was used here). The middle panel shows the effect of delaying the start of pruning until a certain number of trials have been conducted (to avoid prematurely pruning the correct class). Here, we used a fixed p-value threshold of 2×10^{-3} . We observe that as long as we use ≥ 5 steps, the performance is not significantly affected.

The right panel illustrates the impact of the p-value threshold when pruning begins after 20 steps. As expected, performance improves with lower thresholds, approaching the theoretical maximum (the highest value in the left panel) when a value of 2×10^{-4} is used.

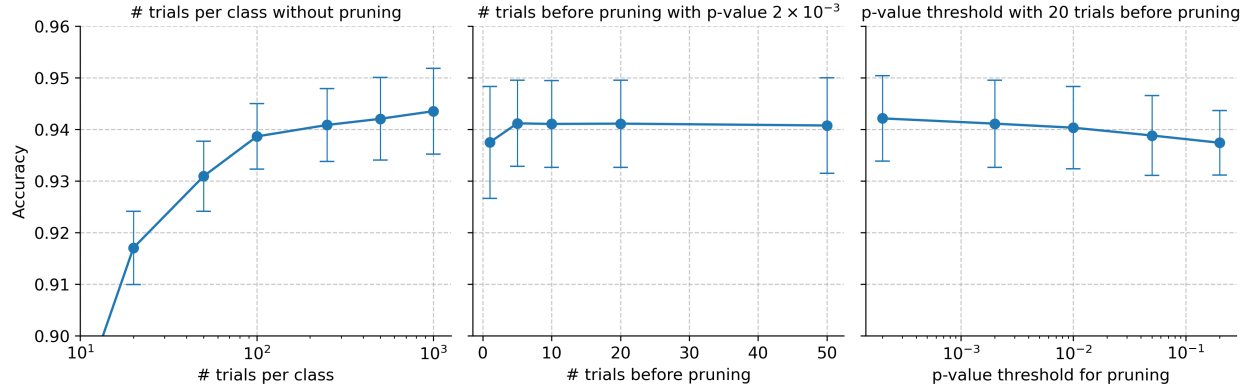


Figure 7: Ablation studies on pruning hyperparameters. Left: Performance vs number of trials per class (no pruning). Middle: Impact of delaying pruning initiation. Right: Effect of p-value threshold on pruning.

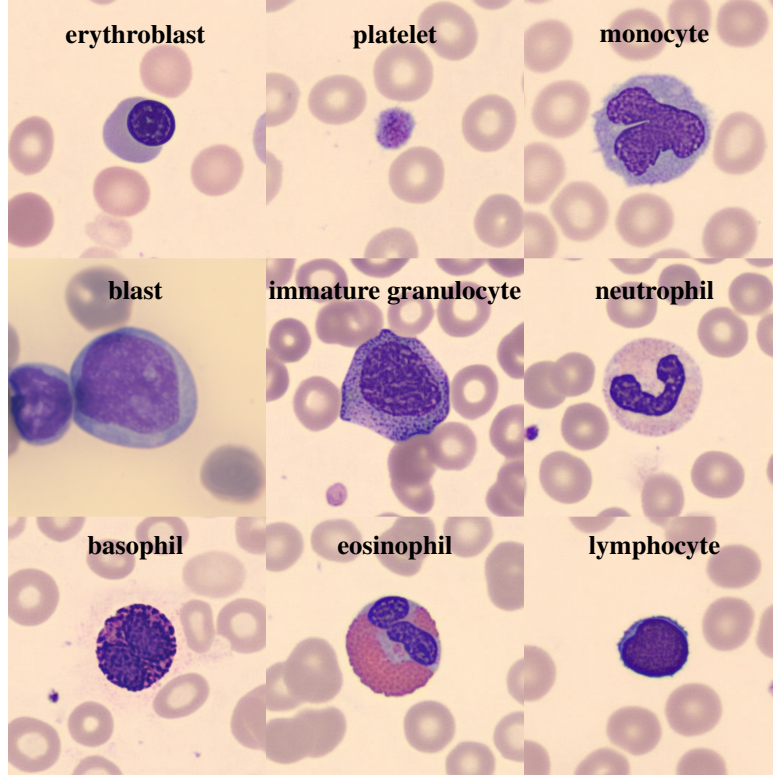


Figure 8: Synthetic blood cell images generated by our fine-tuned diffusion model. The figure displays one synthetic image for each of the nine blood cell classes. These images demonstrate the model's ability to capture distinct morphological features of each cell type.

B Generated Images

The images presented in Figure 8 showcase the capability of our fine-tuned diffusion model to generate highly realistic synthetic blood cell images. Each image in the grid represents one blood cell class. These synthetic images were part of the dataset used in the Turing test described in the main text, where expert haematologists were unable to reliably distinguish them from real blood cell images.

C Labeller Confidence Analysis

To provide insight into the consistency of labeller confidence across different experts, we analysed the agreement between labellers when assessing the same images. Figure 9 presents a confusion matrix of labeller confidence scores based on a subset of our dataset.

For this analysis, we used a set of 200 images that were independently labelled by all six expert haematologists in our study. We then evaluated their confidence levels pairwise, resulting in 30 comparisons per image.

The matrix reveals a strong tendency for labellers to agree on high-confidence assessments, as evidenced by the large number (2,556) in the top-left cell. However, there is also notable disagreement in some cases, particularly between high and moderate confidence levels.

Interestingly, instances of ‘No Confidence’ are relatively rare and often do not align with other labellers’ assessments. This could indicate that factors leading to a complete lack of confidence are highly subjective or dependent on individual expertise.

These findings underscore the complexity of expert assessment in haematological image analysis and highlight the potential value of incorporating confidence measures in models to go beyond expert human behaviour.

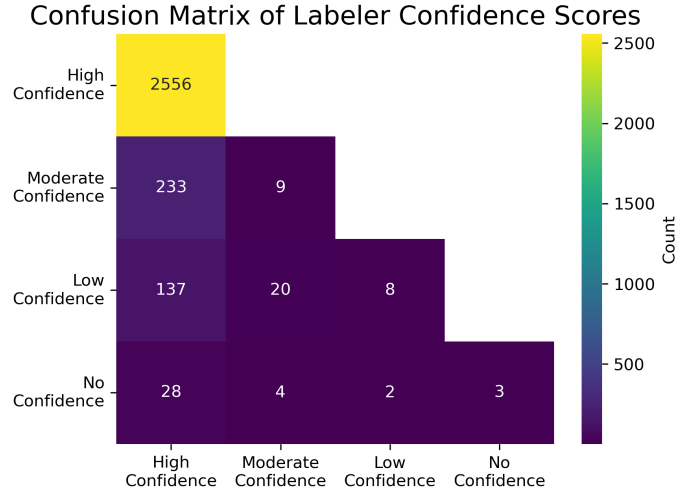


Figure 9: Confusion matrix of labeller confidence scores. The matrix shows the frequency of agreement and disagreement between different labellers’ confidence levels when assessing the same 200 images. Each cell represents the count of pairwise comparisons (out of 3,000 total comparisons) where the confidence levels of two labellers aligned as indicated. The diagonal represents agreement, whilst off-diagonal elements indicate discrepancies in confidence assessments between labellers.

D High-Level Explanation of Model Prediction

For an intuitive explanation of how our model makes its predictions, we refer to Figure 10. This figure presents a toy example demonstrating how the model determines whether an original image depicts a kitten or a puppy.

The process begins by adding noise to the original image. This noisy image is then fed through the model twice: once with the condition that it is a kitten (that is, the model is told that it is an image of a kitten), and once with the condition that it is a puppy. For each condition, the model predicts how to transform the noisy image into an image of either a kitten or a puppy, respectively.

The model then compares the original image with the created images for the different classes. The class that produces the image most closely matching the original is selected as the model’s prediction.

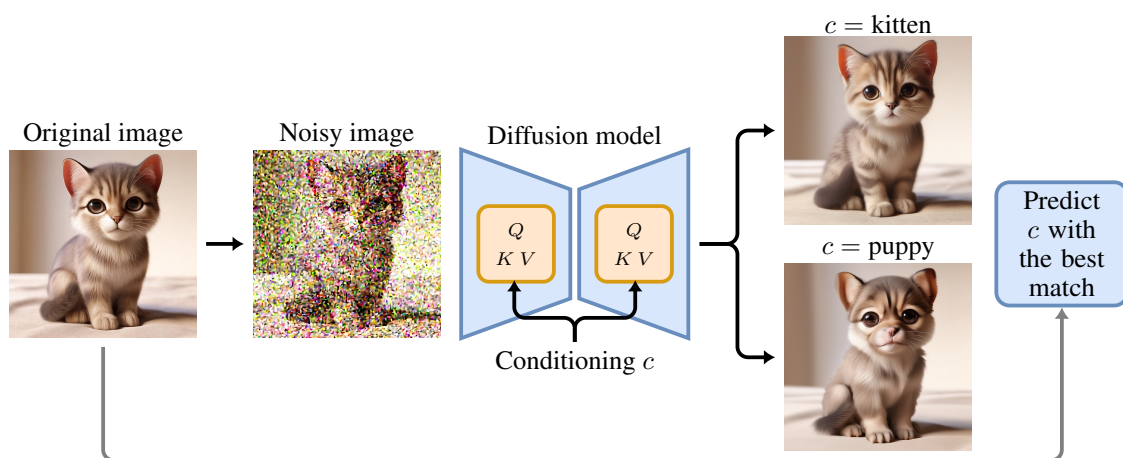


Figure 10: High-level overview of how the model predicts a class.